On identifying natural frequencies in the JAST80 telescope and validation with a simplified 3D model

Fernando Arranz, Javier Abad, Pedro Ramos, Samuel Bielsa, Axel Yanes-Díaz and Guillermo Palacios-Navarro

***Abstract*—The instrumentation of professional telescopes is very sensitive to vibrations. These vibrations, caused by wind, terrain, or its actuators, affect the quality of the images taken. If vibrations present frequency components coinciding with the natural frequencies associated with the proper modes of the telescope mount, the vibratory response is amplified and cause a decrease in image quality below the required standards. The goal of our study is to identify the natural frequencies of the Equatorial-German mount of the JAST80 telescope of the Observatorio Astrofísico de Javalambre (OAJ) and to validate a simplified Finite Element Model (FEM). In addition, the interaction of the vibrations produced by the actuators in a right ascension (RA) movement with the natural frequencies obtained by means of a Finite Element Analysis (FEA) is analyzed. To excite the structure of the telescope, the response of it in free vibration after an unexpected emergency stop of an RA movement was used. A setup of three accelerometers allowed us to compare the excitation frequencies of the structure with those obtained with the FEA. Natural frequency values obtained through the FEM showed deviations below 12% with respect to the experimental values, thus validating the simplified 3D numerical model of the telescope mount for further analysis of its dynamic behavior. On the other hand, the analysis of the measured vibratory indicated that the natural frequencies of the mount for a RA movement in normal operation were not excited by the actions produced by the actuator and therefore the quality of the images taken is not compromised. Finally, the possibility of using the measurement of the vibrational response of the mount in emergency stop conditions to monitor its structural integrity is pointed out.**

***Index Terms*— Finite Elements Analysis, Finite Element Model, resonance frequency, telescope, modal forms.**

This This paragraph of the first footnote will contain the date on which you submitted your paper for review, which is populated by IEEE.

F. Arranz is with the Electronic Engineering and Communications Department, University of Zaragoza, Teruel, 44003 Spain (e-mail: farranz@unizar.es).

J. Abad is with the Mechanical Engineering Department, University of Zaragoza, Zaragoza, 50018 Spain (e-mail: javabad@unizar.es).

P. Ramos is with the Electronic Engineering and Communications Department, University of Zaragoza, Teruel, 44003 Spain (e-mail: pramos@unizar.es).

S. Bielsa is with the Observatorio Astrofísico de Javalambre (OAJ), Centro de Estudios de Física del Cosmos de Aragón. Teruel, 44001 Spain (e-mail: sbielsa@cefca.es)

A. Yanes-Díaz is with the Observatorio Astrofísico de Javalambre (OAJ), Centro de Estudios de Física del Cosmos de Aragón. Teruel, 44001 Spain (e-mail: ayanes@cefca.es)

G. Palacios-Navarro is with the Electronic Engineering and Communications Department, University of Zaragoza, Teruel, 44003 Spain (e-mail: Guillermo.palacios@unizar.es).

I. INTRODUCTION

OPTICAL telescopes are astronomical instruments that let us access to the observation, measurement and record of distant objects and events located outside the Earth's atmosphere. Telescopes capture electromagnetic radiation, being able to carry out measurements with a higher level of detail and precision than through direct observation.

However, ground-based professional telescopes are extremely sensitive to vibrations that could affect the quality of the images taken. Regarding the origin of the oscillations, the sources of vibration can be external or internal to the telescope [1]. As for those of external origin, we can consider as an example those produced by the emplacement -or pier [2], [3]- on which the observatory is located; or by wind-buffeting, which especially affects large surfaces such as the dome that normally covers the observation system [3], [4], [5]. On the other hand, vibrations can be originated in the moving parts of the telescope, such as motors, actuators or auxiliary instrumentation systems. Thus, a high-precision motion control system is essential to deal with problems such as mechanical resonances, friction torque, etc.

Regardless of the origin of the vibration, it is essential to know the natural frequencies -also named characteristic or resonance frequencies-, and the vibration modes of a structure. Then, when a system is excited at one of its characteristic frequencies, its vibration suffers an amplification effect, because the stiffness and the inertial forces of the system tend to cancel each other. The natural frequencies of the pier also affect the performance of an optical telescope. Lammen et al. [6] experimentally determined the frequencies and natural modes corresponding to the Secondary Mirror Assembly, as well as by means of a finite element model, with the aim of identifying and evaluating solutions to the existing resonance problem. Gatkine and Kumar, in their study [2] obtained the resonance frequency of the large pier supporting a 3.6 m telescope to ensure that the resonance frequency of the pier was well apart from those of the telescope fixtures. They could then evaluate the undesired energy transference from the pier to the optical system. In [3], the first natural frequency of the telescope pier is measured by experimental methods. In so doing, authors verify that the measured value (14.3 Hz) is above the imposed limit of 10 Hz.

The natural frequencies and vibration modes of the structure are identified by detecting the peaks of the frequency response of the system model and using modal analysis techniques [2]. One may find in the literature modal analysis simulations carried out to obtain up to the lowest 200 modes [5], whereas other researches are focused just on the three lowest modes

[7]. Structural analysis and finite element analysis is often used in design-oriented tasks to meet a standard requirement: the minimum resonant frequency must be above a cut off frequency [2], [8]. In the research here presented, we calculate and compare by two different methods –numerical modal analysis and spectral analysis of the measured vibrations- the first six modes. The justification for limiting the number of frequencies to be studied to six is based on the fact that 80% of the mass of the structure is mobilized with these six modes.

Obtaining a model of a system that provides its natural frequencies is essential to predict its behavior. A model is a theoretical abstraction of reality aimed at facilitating its understanding and carrying out a realistic performance assessment. When a model is developed, we must take into account the trade-off stablished between fidelity -models must be sufficiently precise- and tractability -simple models are preferred-. In the case of a system as complex as a professional telescope, having a reliable and manageable model allows us to estimate the quality of the images taken or to carry out preventive maintenance tasks, all without having to develop intrusive actions in an equipment whose use is conditioned by numerous research projects that leave few free time slots for maintenance and control tasks. In a further step, one could even consider the design and implementation of a 3D self-calibration method on the basis of the continuous spectral analysis of the vibration measurements, as those proposed and compared in [9].

Having a precise model also allows the development of low-frequency resonance rejection strategies based on active techniques [10]. In [4], a complete parametric model of the dynamic performance of an optical telescope is presented. This research not only includes a parametric description of the structural dynamics, but also of the wind, the active control system and the optical response of the telescope.

The telescope on which this research work is based is the JAST80 (Javalambre Auxiliary Survey Telescope). It is a Ritchey Chrétien type telescope of 80 cm with a field of view of 2-degree in diameter. It is located in the Observatorio Astrofísico de Javalambre (OAJ, Teruel, Spain). Its location has excellent conditions for astronomical observation, especially in terms of seeing and the darkness of the night sky. The facility depends on the Centro de Estudios de Física del Cosmos de Aragón (CEFCA) and is catalogued by the Spanish Government as a Singular Technical Scientific Facility (ICTS). The telescope is part of the ambitious project aimed at obtaining the largest stellar map in the northern hemisphere. The CEFCA project includes two complementary tasks developed in two twin facilities: the Javalambre Photometric Local Universe Survey (J-PLUS) [11], carried out by OAJ, and the South Photometric Local Universe Survey (S-PLUS), developed in Cerro Tololo Inter-American Observatory (CTIO) in Chile [12].

The German equatorial mount is the supporting structure of the JAST80 telescope. This mount is based on the use of two perpendicular axes. The first of the axes allows the movement known as declination (DEC) and the second axis, which must be placed parallel to the rotation axis of the Earth, allows the movement in right ascension (RA). To correctly align the structure, the latitude of the telescope site must be taken into account. The German equatorial mount uses the projection of the parallels and meridians on the celestial dome as a reference, making it the most suitable mount for observing celestial objects. Regarding the positioning speed, in the initial phase, known as slewing, the positioning movement is fast until the telescope is oriented towards the object to be followed. However, when one wants to track the celestial object already located, the telescope starts a movement at a lower speed known as tracking. In [13], it was observed that the movement in declination has less impact on the vibrations in the JAST80 CCD than the movement in right ascension. The start and stop movements in slewing mode naturally produce a higher level of vibration in the structure than in tracking mode, due to its inherent higher acceleration.

In this work, a three-dimensional model of the support structure of the telescope is presented. The model is used to obtain the natural frequencies of the system. The model has been simplified by reducing some of the real parts of the system to highly simplified elements represented as punctual weights. In the simulation, the analysis of the effect of the dome and the concrete pier has also been omitted. In addition, some minor details of the pieces have been left out. These simplifications reduce significantly the computational costs of the finite element analysis. In the literature we can found researches aimed at saving computational expenses so as to run simulations in a standard computer; for instance, in [5], Zhao Fu et al. use the lattice Boltzmann method in a computer simulation package with a reduced computational complexity to study the dynamic impact of the wind on a 2-meter telescope. Concerning the simplification of models, in the context of the Lira-B experiment developed aboard the International Space Station (ISS) [14], a simplified model was used in simulations providing results in good agreement with those obtained from the real complex model. We have reduced the mesh density of the finite element analysis of the model to reduce run time. A similar approach was successfully performed by Worthington et al. [7].

As far as the software tools are concerned, the 3D model has been developed using SolidWorks. This software tool is broadly used in simulations in this field [2], [5], [7], [14], [15].

Different experimental analysis techniques can be found in the literature to obtain the natural vibration frequencies of a structure: impulse response, response to harmonic excitations or random vibration. We must emphasize that, although in some experiences carried out in other laboratories, measurement strategies based on the external excitation of the system through actuators have been performed, in our case, given the characteristics of the equipment, we cannot propose similar methods since they could cause damage or misalignment to the equipment.

As it has been pointed out, due to the singularity of the structure under study, we have proposed in this work to experimentally identify its natural frequencies, taking advantage of the free vibration to which it is subjected after an emergency stop. Therefore, a frequency analysis will allow us to identify them, in a similar way as indicated in the study of Lim et al. [16]. In their work, the response of a bridge subjected to a transient excitation was measured by examining the vibratory response, in free vibration, by means of an array

of accelerometers and performing the FFT on the temporal signal to identify resonant frequencies [16]. The spectral analysis of the signals, performed by the simple FFT or Short Time Fourier Transform (STFT), will be carried out with the help of MATLAB software. The STFT analysis has been already used to determine and identify harmonic components [17], whereas the MATLAB software has been used by researches in the field, like the modeling and the dynamic analysis of the Large Synoptic Survey Telescope at Cerro Pachón, Chile [15].

On the other hand, a spectral analysis of the forced vibration in normal operating mode will help us to observe if the most relevant frequencies of the measured vibration correspond to the natural frequencies of the structure. Frequency-domain estimators based on the discrete Fourier transform (DFT) have been used [18] and analyzed [19] in different contexts.

Therefore, our main objective is to identify the natural frequencies in the JAST80 telescope and their validation with a simplified 3D model. To achieve this objective, four secondary objectives were set. First, we measured the vibration in the JAST80 instrumentation in free vibration after emergency stop of the mount and spectral analysis by means of the FFT of the measured signals. Second, we obtained the modes and natural frequencies by FEA of the simplified FEM model of the telescope mount. Third, we compared the frequencies obtained from the spectral analysis with the natural frequencies obtained from the FEA to validate the simplified FEM model. Fourth, the spectral analysis of the AR movement in normal operation and its interaction with the natural frequencies of the structure was performed.

The paper is organized as follows: In section 2 the telescope and its supporting mount are described. Besides, spectral analysis tools and the FEA strategies are presented. In section 3, we present and compare the natural frequencies of the system obtained by both methods: FEA of the simplified model and spectral analysis of the measured signals. The main ideas are discussed in section 4, whereas final conclusions are drawn in section 5.

II. Materials and Methods

A. JAST80 mount

The JAST80 has a 6.25 m diameter hemispherical dome and a 1.8 m wide opening. The dome is seated on a rail with wheels that rotates 360º simultaneously and in the same direction as the telescope is positioned. Below, there is the technical floor for maintenance work with access to lower floors (see fig. 1). The telescope is fixed to a concrete pier cemented to the ground with a height of 4.5 m and a diameter of 1.5 m. It is mechanically isolated from the structure of the OAJ building in order to avoid the transmission of vibrations through the ground.

The German equatorial mount is designed for the geographic location of the OAJ. The lower inclination angle of the base is the one necessary to align the center of the upper cone with earth rotation axis, which is the same axis prolongation passing as well through a known spatial point located quite next to the polar star, while the upper angle of the mount is 90° (see fig. 1). It has a frusto-conical shape from the base to the 2B flange, it is hollow inside and houses the wiring and service facilities. It is made of 5 mm thick steel sheets joined by welding cord throughout the structure. The fixing to the pier is done with threaded bars embedded in the concrete and nuts at the base of the platform.

Fig. 1. JAST80 telescope and description of movements.

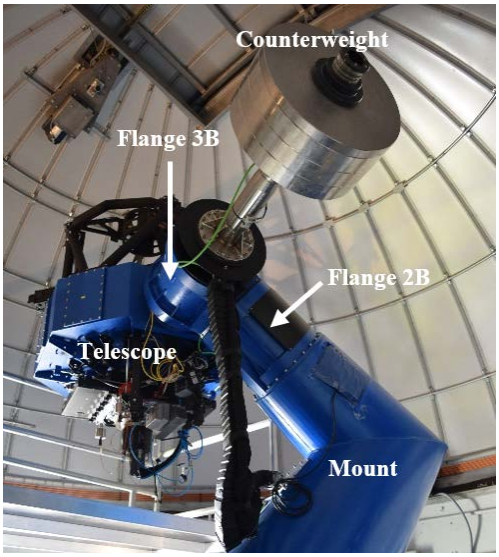

Fig. 2. Telescope JAST80, mount and location of 2B flange, 3B flange and counterweight.

The 2B flange acts as a union between the mount and the 3B flange (see fig. 2). 2B flange houses inside a direct transmission “brushless torque motors” for the right ascension (RA) movement. The elimination of intermediate transmission mechanisms between the motor and the flange favors the precision of the positioning and the removal of clearances due to mechanical coupling.

The flange 3B is associated at one end to the telescope by means of the "brushless torque motors" in charge of the declination (DEC) movement and at the opposite end to the counterweight. The counterweight bar itself and counterweights balance the torque of the motor in the RA movement, attenuating the starting and slowing down torques.

In other words, motor torque is mainly affected by inertia momentum and friction contributions. In the event of motor and brake failure, the telescope and counterweights will remain in balance, avoiding movements due to gravity vector.

The telescope has a Ritchey-Chrétien optical configuration with Cassengrain focal plane and field corrector. It is made up of an 80 cm diameter hyperbolic primary mirror (M1) with a 2-degree field of view and a secondary mirror (M2) with an active hexapod optics. It is associated with the T80Cam instrumentation [13] consisting of a "Filter and Shutter Unit" (FSU) and a Charged-Couple Device (CCD) detector with a matrix of 9.2 k x 9.2 k pixels of 10 µm size with an ideal maximum acceleration limit of 1G.

The telescope has two degrees of freedom (DOF) perpendicular to each other for location and positioning. In the DEC movement, the telescope rotates on the 3B flange axis in alignment with the counterweight bar, while in the RA movement, the telescope and counterweights rotate perpendicular to their alignment axis.

On the other hand, the telescope has two speed modes. In tracking mode, the telescope moves in RA and DEC at the same speed of earth rotation for sidereal tracking. During the exposure time, the telescope stays focused with the celestial body. In slewing mode, the telescope is moved from location to a new observation, parking or maintenance position. In the latter, the speed is considerably higher than in the former mode.

The "brushless torque motors" actuators on 2B and 3B flanges are controlled by the ETEL-DSC2P903 commercial drive. The regulator is programmed with an s-curve profile, smoothing the transitions of the acceleration trapezoidal profile, protecting the instrumentation from excessive accelerations [13].

B. Instrumentation and set-up

The installed setup was already used by Arranz et al. [13] on the JAST80 to determine the maximum displacements that occur in the CCD as a consequence of the vibrations in slewing mode. It consists of 3 Wilcoxon model 731A piezoelectric accelerometers with dynamic signal output, frequency range between 0.05 Hz and 450 Hz and 10 V/g sensitivity. They are connected to a 4-channel National Instruments NI9234DAQ data acquisition card with integrated electronics piezo-electric input. The converter is a Delta-Sigma type with a range of up to 51.2 kS/s and 24-bit ADC resolution. The card connects to a National Instruments model NI-cDAQ-9148 8-slot input/output chassis and an Ethernet communication port with a 10 MHz/100 MHz communication range. The accelerometers have a 62.23 mm diameter and they are 73.40 mm in height with a weight per accelerometer of 760 g. They are attached to the FSU by 4 threaded fixings (Fig. 3).

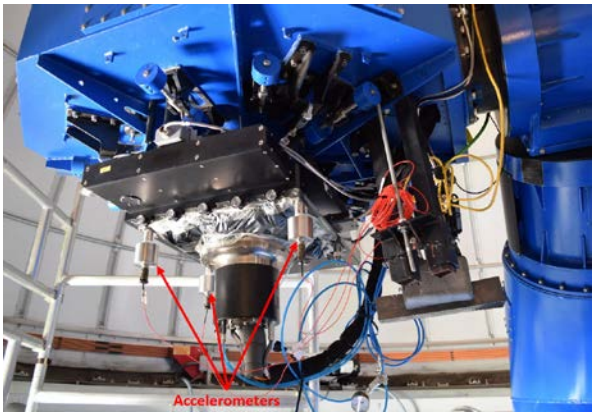

Fig. 3. Set of accelerometers on the FSU next to the CCD

The acquisition of signals and offline processing begins by accessing the CEFCA-OAJ via a virtual private network (VPN). The connection to the chassis requires the NI Max v20.0 application for hardware parameter configuration. The signal management and processing software used is Matlab r2021b together with the "Analog input recorder" Toolbox. NI Max runs to establish communication with the chassis while Matlab r2021b software records and processes the data.

C. Signal analysis tools

The discrete-time Fourier transform $X(\omega)$ of a sequence $x(n)$ is a complex-valued function of the continuous variable ω. $X(\omega)$ is a periodic signal that indicates how much of each frequency component is required to synthetize $x(n)$.

Provided that in practical applications one may deal with a finite number L of data to represent a signal, the discrete Fourier transform (DFT), denoted as $X(k)$, provides N samples of $X(\omega)$ by a discretization given by:

$$X(k) = X(\omega)\big|_{\omega=\frac{2\pi}{N}k} \quad k = 0, \dots, N-1 \qquad (2)$$

Finally, the fast Fourier transform (FFT) is just a computationally efficient implementation of the DFT.

Then, as far as the size N of the FFT algorithm is concerned, the selection N determines the spectral resolution. The trade-off defined by the selection of this parameter is clear: the larger N is, the better the spectral resolution is but, –as a drawback– the higher the computational complexity is.

We focus our attention on the parameters' adjustments that one must carry out in order to obtain accurate measurements in the frequency-domain.:

- L, the length of a discrete-time signal $x(n)$,
- N, the size of the FFT, and
- the type of window used

The level between the main lobe and the side lobes cannot be maximized by changing the length of the rectangular window. Nevertheless, it can be improved by choosing a different type of window. Other windows propose a trade-off between the width of the main lobe and the ratio main/side lobes. To accomplish that, we analyze the responses of 5 types of windows, rectangular, Barlett, Hanning, Hamming and Blackman window, respectively. Fig. 4 shows the secondary lobes in the frequency domain for each window, each of them having its own characteristics for different signal analysis.

Positive effects of adding a step of windowing before carrying out spectral analysis have been widely used [20].

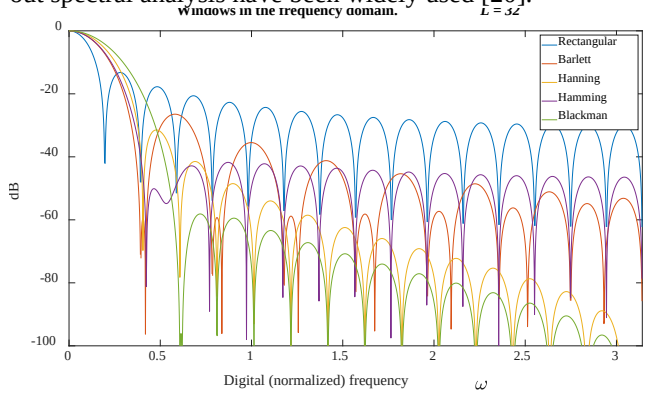

Fig. 4. Windows in the frequency-domain.

The Fourier transform allows us to decompose a signal and to reconstruct it without loss of information. It provides a good frequency resolution that makes it a very useful tool for the analysis of stationary signals. However, the Fourier transform presents the problem of its inherent inability to correctly analyze signals that are not stationary in time: it cannot be applied to obtain precise information on when the different spectral components appear in the signal. Non-stationary behavior is a common phenomenon that appears in most signals. To overcome this limitation, we refer to a variant of the Fourier tools: the STFT, in which we can analyze the signal and obtain information on both the signal spectrum and the instant of time in which these frequencies are present. Interested reader is referred to [21] to find out more alternatives of instantaneous spectral analysis.

In order to overcome the limitations of Fourier transform tools a different analysis was later introduced. Such an analysis consists in introducing a window function of given length which slides over the time axis to execute a time-localized Fourier analysis of the windowed data. This approach, called the Short Time Fourier Transform (STFT), was first introduced in 1946 by Dennis Gabor [22].

The procedure consists of dividing a signal into small segments of time in such a way that we can assume that for each segment the signal is stationary and, thus, calculate the standard Fourier Transform for each portion of the signal. By means of the window function we frame the signal around an instant of time and calculate its Fourier transform, then we slide the window function, there may be a certain overlap with the previous one, covering a new portion of the signal and we recalculate its Fourier transform. The window hops over the original signal at intervals of R samples. Most windows taper off at the edges in order to avoid spectral ringing. If a non-zero overlap length L is specified, overlap-adding the windowed segments compensates for the signal attenuation at the window edges. The Fourier transform of each windowed portion is added to a matrix that contains the magnitude and phase for each point in time and frequency.

The STFT matrix is given by

$$X(\omega) = [X(\omega,1)\ X(\omega,2)\ \ X(\omega,3)\ldots X(\omega,M)] \qquad (7)$$

such that the *mth* element of this matrix is

$$X(\omega,m) = \sum_{n=-\infty}^{n=\infty} x(n)w(n-mR)e^{(-j\omega n)} \qquad (8)$$

where $w(n)$ is a M-length window function; $X(\omega,m)$ is the Fourier transform of the windowed data centered at time mR; R is the hop size between successive Fourier transforms. The hop size is the difference between the window length M and the overlap length L.

The magnitude squared of the STFT yields the spectrogram representation of the power spectral density of the function. Then, the window function $w(n)$ is used to compute the STFT dividing each the signal into segments of the same length with an overlap between adjoining segments set to the largest integer less than or equal to 75% of the window length. The function then windows each segment with the specified window. It is advisable to check that the window satisfies the constant overlap-add (COLA) compliance. COLA compliance ensures perfect reconstruction for non-modified spectra.

As an example, we represent a signal whose frequency increases with time: $x(t)=cos(2\pi 2(1+\Delta ft)t)$ with two types of windowing: rectangular (see figure 5) and Blackman (see figure 6). At the top of figures 5 and 6 (time domain), we observe that as we move forward in time, the frequency of the signal increases while the amplitude remains constant. In the lower part of figures 5 and 6, the STFT performed on the signal has been depicted (both windows were applied). In both cases, a growth in the frequency is observed given by a slope proportional to Δf. However, the two most important differences derived from the choice of the window are also clearly seen. If a rectangular window is used, the width of the main lobe is reduced, but secondary lobes appear. If, on the other hand, we use the Blackman window, we manage to drastically reduce the level of the secondary lobes until it is negligible, at the cost of increase the width of the main lobe.

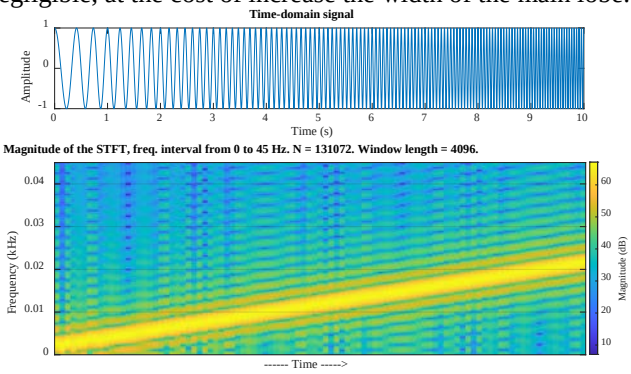

Fig. 5. STFT. $x(t)=cos(2\pi 2(1+\Delta_f t)t)$ rectangular window.

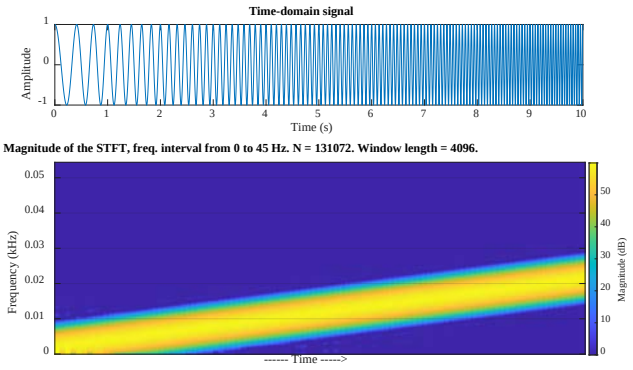

Fig. 6. STFT. $x(t)=cos(2\pi 2(1+\Delta_f t)t)$ Blackman window.

D. Model and numerical analysis

The dynamic response of a structure is determined by the natural frequencies and the associated modal shapes, so it is essential to know them to predict the vibrational response that the mount will undergo when facing to a dynamic excitation. In order to define a numerical model that allows analyzing the vibratory response that the slewing movements generate on the telescope mount, the dome and the concrete pier to which it is fixed are ignored. Therefore, we limit our analysis to the assembly formed by the mount, the drive flanges, the telescope and the counterweights (see fig. 7).

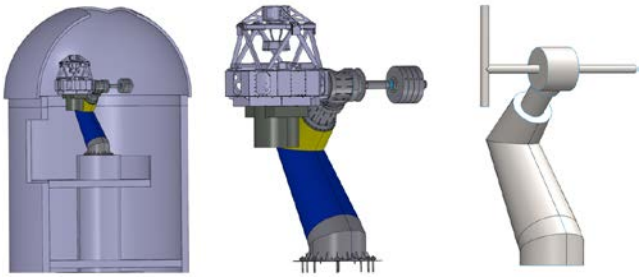

Fig. 7. Simplified 3D model.

However, it is not necessary to make a detailed model of each of these parts, since, considering the frequency range of interest (low frequencies), there are components that act as perfectly rigid elements that only introduce mass to the system [23], [24]. Applying this idea, we consider that the telescope behaves as a rigid element that only introduces mass to the system, as well as the two flanges (2B and 3B) with the positioning and counterweight systems. In this way, we simplify the model without losing accuracy in the analysis [25], as fig. 8 depicts.

With all these premises, we proceed to define the geometry that will serve as the basis for defining the finite element model that allows determining the natural frequencies as well as the vibration modes. For this stage we use the CAD module of the SolidWorks 2021 software.

The geometry is created with surfaces which later are meshed with SHELL-type elements, defining the thickness and the material associated with each of the components that make up the structure as a whole. As we have previously pointed out, the telescope will behave as a rigid solid, characterized by the mass of the three main subassemblies that compose it: spider, primary mirror and instrumentation. We will create a simplified geometry that positions these masses in their equivalent location given by their center of gravity (see fig. 8).

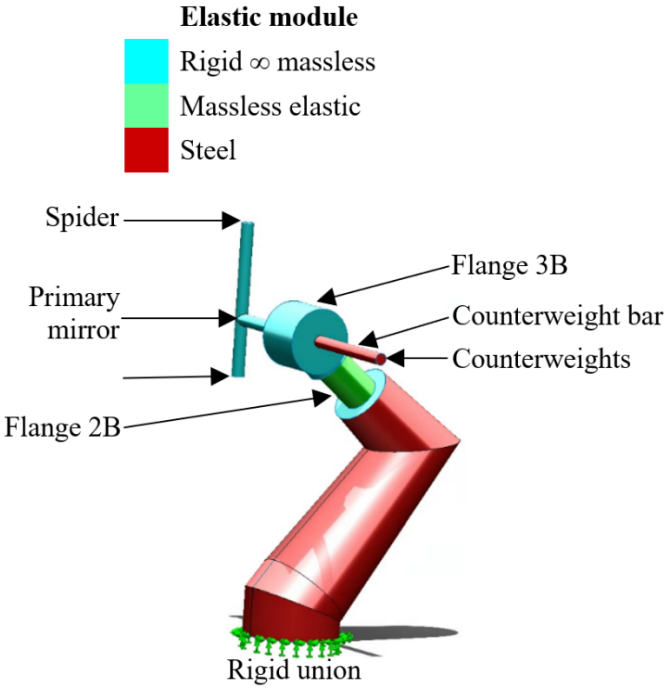

Fig. 8. Material within the 3D model.

First, we associate the materials to each of the parts. Typical values for the steel properties, density (7700 kg/m3), Poisson's ratio (0.29), and elastic modulus (210 GPa) are defined and assigned to the mount and counterweight bar. With ideal rigid material and no density, we define the 3B flange and the simplified structure of the telescope. The 2B flange, due to the uncertainty of its behavior as ideal rigid or flexible due to the AR movement, is established without density, being studied with three different elastic moduli in line with the improvements provided by Gatkine et al. in their study [2].

After that, we linked the masses corresponding to the elements that are considered to have a rigid behavior (spider, primary mirror, instrumentation, counterweights and 2B and 3B flanges) to the geometry through MASS type elements). At this point, since the mass of the primary mirror were not available, it was determined by equilibrium with respect to the axis of 3B flange using equation 9 where *m* is the mass and d is the distance from the CDG of the element to the center of 3B flange.

$$(m_{bar}d_{bar}) + (m_{weight}d_{weight}) = (m_{spider} + m_{primary\ mirror} + m_{instruments})d_{telescope} \quad (9)$$

Table 1 shows the data obtained from the masses and the source from which they have been obtained, while table 2 shows the distances with respect to the axis of flange 3B.

TABLE 1
WEIGHTS OF ELEMENTS

Element	Mass (kg)	Data source
Counterweights	378	Solidworks
Counterweight bar	58	Solidworks
Spider	35	Assigned OAJ
Instrumentation	68	Assigned OAJ
Primary mirror	410	Calculated
Flange 2B	81	Solidworks
Flange 3B	128	Solidworks

The sources of the data in Table 1 come from the calculations from the volume and density of the 3D model material using Solidworks software, assigned by the OAJ engineering team according to their databases (assigned OAJ) and results calculated from equation (9).

TABLE 2
DISTANCES FROM THE COG OF EACH ELEMENT TO THE CENTER OF THE 3B FLANGE

Element	Distance (mm)	Data source
Counterweights	888	Telescope
Counterweight bar	581	Solidworks
Spider	719	Solidworks
Instrumentation	719	Solidworks
Primary mirror	719	Solidworks

The sources of the data in Table 2 are: the telescope (obtained by measuring instruments calibrated directly from JAST80) and the solidworks (measured on the 3D model by Solidworks software tools).

In the next step we define the boundary conditions, restricting the 6 DOF in the lower edge of the mount that allows us to simulate the rigid connection of the mount to the concrete pier (fig. 8). The 6 DOF measurement methods, which includes three rotation angles and three translations, often requires professional instruments and software. Nevertheless, an interesting low cost alternative based on a smartphone can be found in [26]. Finally, we performed the meshing using SHELL-type triangular elements of 3 nodes with 6 DOF each, with a maximum size of 100 mm and a minimum of 25 mm, obtaining a model with 14686 elements and 7554 nodes. Fig. 9 depicts the 3D model meshing.

In the literature one may find similar FEM-based simulations. For instance, K. Fujita and N. Kuramoto [27] also performed FEM calculations on the basis of triangular elements, but for a 2-D problem (investigating the effect of surface roughness on the mechanical alignment of coaxial cylindrical electrodes).

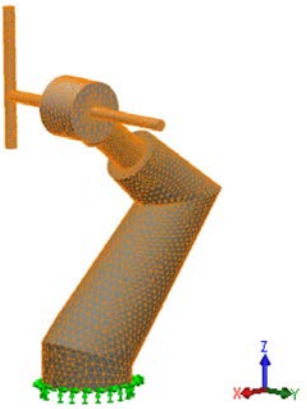

Fig. 9. 3D model meshing.

Once the FEM was defined, we proceeded to determine the first 6 frequencies and vibration modes corresponding to the structure, using the Lanczos iterative algorithm [28].

III. RESULTS

A. FEM Analysis

The first analysis was performed by defining an elastic modulus $E=2\cdot10^{14}$ Pa, similar to an ideal rigid solid for the material associated with 2B flange. The second analysis was performed with an elastic modulus $E=2\cdot10^{11}$ Pa, similar to steel, whereas an elastic modulus $E=2\cdot10^{10}$ Pa (below the typical value of steel) was used in a third analysis. Table 3 depicts the obtained first 6 natural frequencies of the mount.

TABLE 3
FEA RESULTS FOR THE FIRST 6 MODES WITH THREE DIFFERENT ELASTICITY MODULI VALUES AT 2B FLANGE

Modes (Hz)	**Elastic moduli E (Pa)**		
	$2\cdot10^{14}$	$2\cdot10^{11}$	$2\cdot10^{10}$
1st	8.38	7.20	5.80
2nd	9.98	9.07	7.67
3rd	13.92	13.24	8.94
4th	18.46	16.26	13.83
5th	33.58	31.34	24.32
6th	62.78	55.37	39.25

The modal mass participation factor for the intermediate case with an elastic modulus similar to that of steel gives us the result shown in table 4. As it can be seen in table 4, practically 80% of the mass of the structure is mobilized taking into account the first six modes, so it can be considered that the response of the structure is largely conditioned by them.

TABLE 4
MASS DISTRIBUTION

Modes (Hz)	Frequency (Hz)	Direction		
		X (%)	Y (%)	Z (%)
1st	7.20	**32.6**	2.7	0.2
2nd	9.07	2.6	**23.7**	**41.1**
3rd	13.24	6.5	**26.1**	5.8
4th	16.26	14.9	2.4	17.8
5th	31.34	**22.5**	**21.8**	**18.2**
6th	55.37	7.8	0.4	0.5
	Sum	86.9	77.1	83.4

For each natural frequency, the associated modal pattern is obtained, which corresponds to the way in which the structure deforms when it vibrates at that frequency, as shown in fig. 10.

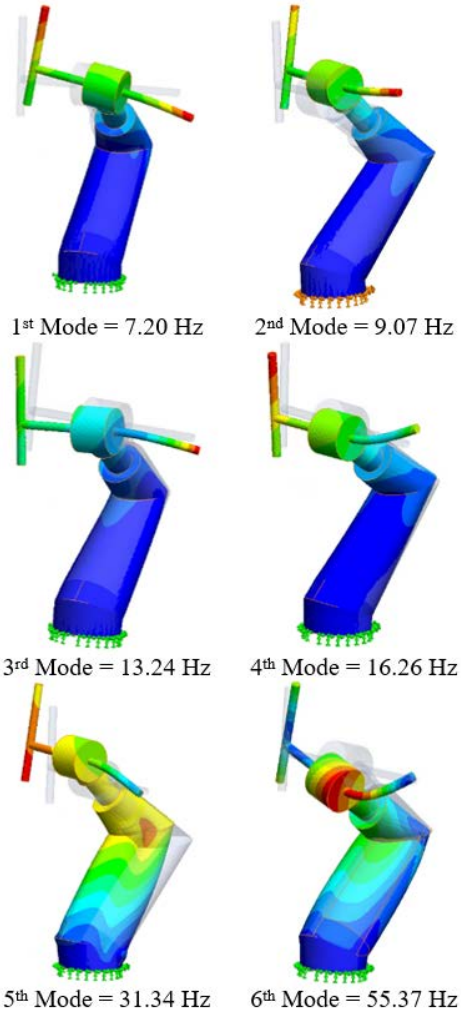

Fig. 10. Deformation graphs according to frequency mode with an elastic modulus similar to steel (E=2 1011 Pa).

Each figure represents in color from coldest to warmest the deformation in relative values. Cold colors imply little or no deformations while warm colors represent larger deformations. At the same time, the gray shaded image represents the initial position of the 3D model without excitation.

B. Signal Analysis

To compare the measurements taken by the accelerometers with the natural vibration modes of the structure calculated from the FEA, we need an unforced motion with free oscillation. This situation of vibration according to the natural pattern of the structure occurs when, for different reasons, an emergency stop, or a similar situation occurs and the structure is left vibrating freely.

We considered a set of signals from different movements in RA and slewing mode. In this set, there were two internal errors with an abrupt stop, so they served as the basis for the experiment. To achieve adjusted FFT results as provided above, we performed multiple experiments looking at different effects.

The first effect to be highlighted is that reducing the size of the window widens the main lobe of each frequency component. This effect is well observed in Fig. 11 and 12, where the time window is reduced from 60 to 1 second. In these figures we apply a rectangular window in both cases. The frequency interval shown is 20 Hz, not too wide, to see the detail in the width of the main lobes.

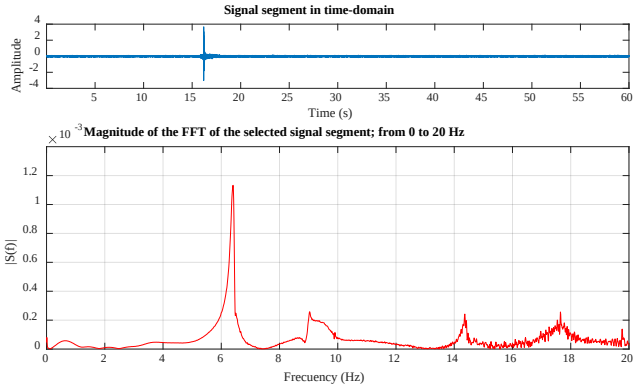

Fig. 11. Signal 1. Upper part, time-domain. Lower part, frequency-domain: Spectrum of a signal segment. Rectangular window; Length of the window *Lw* = 60 s; Displayed bandwidth *Bw* from 0 to 20 Hz.

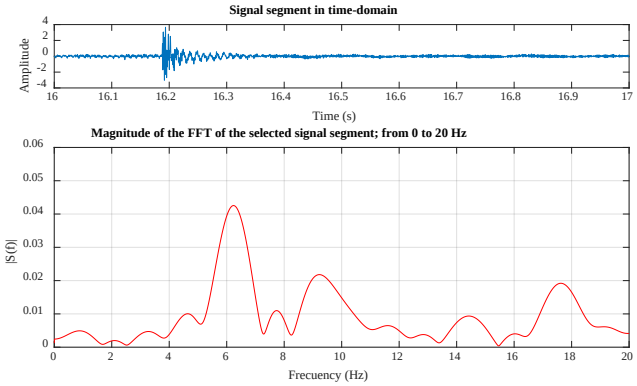

Fig. 12. Signal 1. Upper part, time-domain. Lower part, frequency-domain: Spectrum of a signal segment. Rectangular window; *Lw* = 1 s; *Bw* from 0 to 20 Hz.

Analyzing the effect of the length of the rectangular window in Fig. 13, we extended the frequency range to 60 Hz., above the frequency of 6th mode obtained in the FEA.

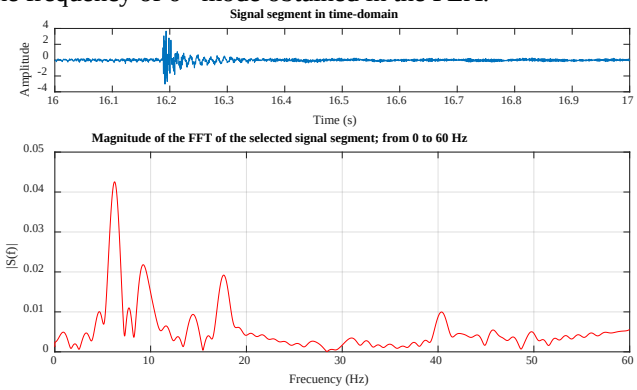

Fig. 13. Signal 1. Upper part, time-domain. Lower part, frequency-domain: Spectrum of a signal segment. Rectangular window; *Lw* = 60 s; *Bw* from 0 to 20 Hz.

The second effect deals with the type of window. Fig. 14 illustrates the effect of 5 types of windows. Namely, rectangular, Bartlett, Hanning, Hamming and Blackman windows, respectively.

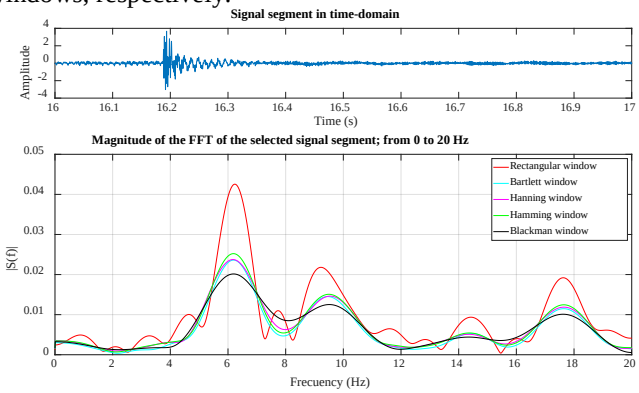

Fig. 14. Signal 1. Upper part, time-domain. Lower part, frequency-domain: Spectrum of a signal segment. Rectangular, Bartlett, Hanning, Hamming and Blackman windows; *Lw* = 1 s; *Bw* from 0 to 20 Hz.

When comparing the different windows, we observe that the rectangular window is the best in terms of the width of the main lobe but the worst in terms of the level of secondary lobes, which are maximum and can lead to error. The Blackman window is the worst in terms of the width of the main lobe, which is maximum, but the best in terms of the level of secondary lobes, which are almost negligible. Additionally, we programmed a peak detector that locates those frequencies in which the spectrum of the measured signal presents some local maximum. To use the detector, we determine the minimum threshold from which we detect the local maxima.

Figures 15 and 16 show two movements with a sudden emergency stop. Figure 15 shows signal 1 with AR displacement from 0º to 90º, DEC from 40º to 40º and acceleration 0.2454 degrees/s^2, while in signal 2 an AR displacement from 0º to 40º and DEC from 40º is programmed at 40º and acceleration 0.179 degrees/s^2.

Both signals are represented with the same windowing parameters, window length and bandwidth.

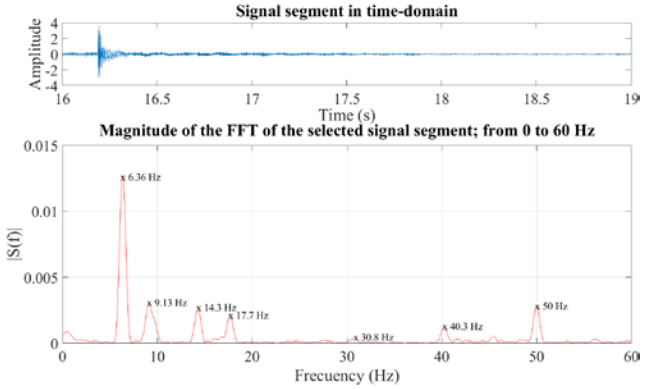

Fig. 15. Signal 1. Upper part, time-domain. Lower part, frequency-domain: Spectrum of a signal segment using the peak detector. Blackman window; *Lw* = 3 s; *Bw* 0 to 60 Hz.

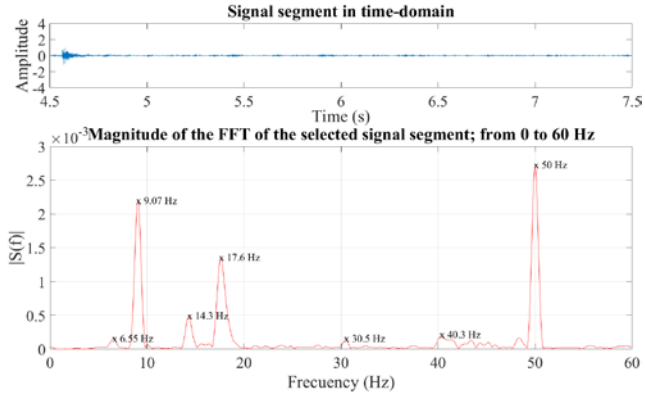

Fig. 16. Signal 2. Upper part, time-domain. Lower part, frequency-domain: Spectrum of a signal segment using the peak detector. Blackman window; *Lw* = 3 s; *Bw* 0 to 60 Hz.

It should be noted that the 50 Hz peak that appears in figs. 15 and 16 is due to the coupling of the frequency of the electrical supply network in the connection cables of the accelerometers with the data acquisition card. To analyze the accelerometer signals of a constant AR and DEC movement in slewing mode, we used the STFT. This tool allowed us to know what frequencies are occurring at each instant of time of the signal, as depicted in fig. 17.

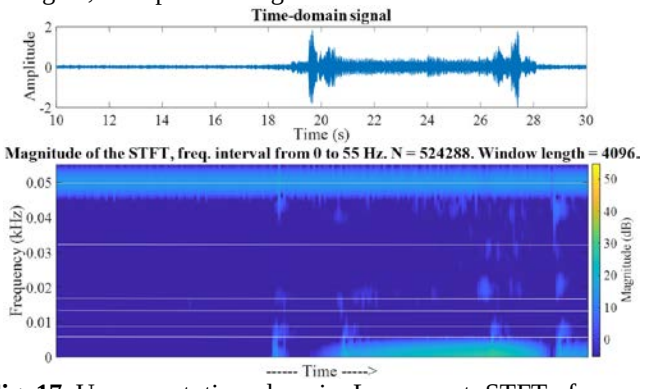

Fig. 17. Upper part, time-domain. Lower part: STFT of a vibration signal segment. Blackman window.

The white lines indicate the 6 calculated frequency modes of the FEA.

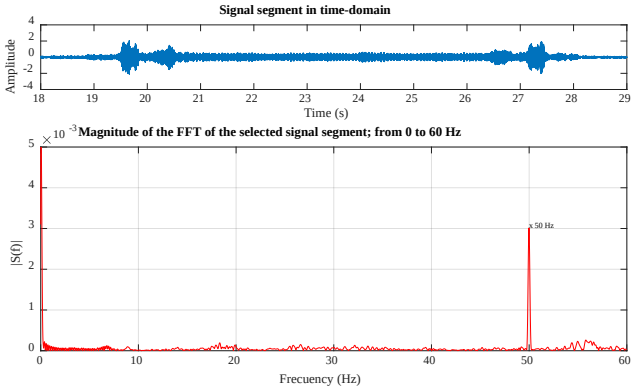

Fig. 18. Upper part, time-domain. Lower part, frequency-domain: Spectrum of a signal segment using the peak detector. Blackman window; *Lw* = 11 s; *Bw* 0 to 60 Hz.

Figure 18 represents the FFT of AR movement under normal conditions in the frequency domain. We observe how the remarkable frequency in amplitude corresponds to the 50Hz of the frequency of the electrical supply network. Finally, Table 5 shows the comparison (percentage differences) of the three experiments carried out with the different elastic moduli between the FEA (shown in Table 3), and the frequencies obtained from spectral analysis through the FFT over signal 1 (fig .15).

TABLE 5
COMPARISON OF NATURAL FREQUENCIES FROM SPECTRAL ANALYSIS AND FEA

	Frequency spectral analysis	$E=2\cdot10^{14}$ Pa		$E=2\cdot10^{11}$ Pa		$E=2\cdot10^{10}$ Pa	
		Frequency mode (Hz)	Difference (%)	Frequency mode (Hz)	Difference (%)	Frequency mode (Hz)	Difference (%)
1st Mode	6.36	8.38	24.11	7.20	**11.67**	5.80	-9.66
2nd Mode	9.13	9.98	8.52	9.07	**-0.66**	7.67	-19.04
3rd Mode	14.30	13.92	**-2.73**	13.24	-8.01	8.94	-59.96
4th Mode	17.70	18.46	4.12	16.26	-8.86	13.83	-27.98
5th Mode	30.80	33.58	8.28	31.34	**1.72**	24.32	-26.64
6th Mode	40.30	62.78	35.81	55.37	27.22	39.25	-2.68

IV. DISCUSSION

The aim of this work was to identify the natural frequencies of the JAST80 telescope mount using a 3D model. The validation of results was carried out, on one hand, with the natural frequencies of the mount obtained from the FEA analysis of a simplified 3D model and, on the other hand, obtaining the most relevant frequencies from the spectral analysis of the vibrations measured with the accelerometers installed in the instrumentation. Subsequently, we analyzed the influence of the resonance frequencies calculated in a movement in normal operation using the STFT tool of the accelerometer signals.

A. 3D model simplification.

Like in Giagopoulos et al.'s work [23], where a point mass to simulate the total mass of a structure was used, or Langer et al.'s work [24], where several FEAs were carried out on a structure in which a part of the assembly was simulated as a point mass located in its CDG, it has been found that considering only the mass of those components that behave as perfectly rigid elements in our 3D model does not affect the accuracy of the results. This result is also consistent with the work of Smekalin et al. [14]. Furthermore, the computational cost is dramatically reduced, fact also pointed out by Thakur et al. in their work [25].

B. Experiments and analysis of FEA results.

The results obtained from the FEA with the simplified 3D model showed the first 6 modes and natural frequencies that define the dynamic behavior of the Equatorial-German mount. In order to adjust the value of the stiffness corresponding to the 2B flange, which provides the movement in AR, a sensitivity study was carried out on the elastic modulus that the 2B flange has on the natural frequencies of the structure, in a similar way to the one used in the work of Gatkin et al. [2]. We repeated the experiment with 3 different elastic modules: the first one equivalent to a rigid material, the second one equivalent to steel and the third one was more flexible than steel.

Table 3 shows the values of the natural frequencies of the FEA with the three elastic modules used. It can be seen that the greater or lesser stiffness of the 2B flange notably influences the natural frequencies of the structure as a whole. A greater rigidity in the flange 2B makes the natural frequencies obtained higher, and on the contrary, the lower the rigidity of such flange, the lower the rigidity of the structure.

When analyzing the results of table 4, we see how 1st mode mobilizes the greatest amount of mass of the total in the X axis. 1st mode together with 5th mode mobilize more than half of the modal mass in that direction. 2nd mode, 3rd and 5th modes share, practically in the same percentage, the total mobilized mass in the Y axis, adding between the three more

than 70% of the modal mass in such direction. 2nd mode stands out, which by itself mobilizes most of the mass in the Z axis, which together with 4th and 5th modes mobilize more than 75% of the modal mass in that direction. As shown in figure 10, this mode corresponds to a bending movement of the upper part of the mount on which the telescope is fixed. This result is very significant if we take into account the direction of Z axis (figure 9), which coincides with the direction of measurement of the accelerometers.

Finally, note that 6th mode presents very low values of mobilized mass in the Y and Z directions, so its influence on the response of the structure in these directions can be ignored.

C. Spectral Analysis

We have performed several experiments using the FFT tool [2], [13], optimized with the adjustment parameters and type of windowing.

The sample length of the signal *L* has been adjusted at the beginning and end of the event to obtain the frequencies of the movement signal (figures 11 and 13). On the other hand, the size of the FFT *N* (FFT length) moves in the compromise between spatial resolution and computational cost. The size of the length of the spectral window (figure 13) was also adjusted to the maximum value of the frequency of 6th mode obtained in the FEA.

The influence of the type of windowing highlights the importance of your choice. It has been found that a rectangular filter has the main lobe with width and amplitude similar to the secondary lobes causing nearby main lobes to be seen as a single one. On the other hand, the Blackman filter, presents a relationship between amplitude and width of the main lobe differentiated from the secondary lobes for the given case, which is why it is the most appropriate in the comparison.

The spectral analysis was complemented by a programmed peak detector identifying the maximum frequency values.

D. FEA results vs spectral analysis.

Two experiments were carried out on the JAST80 with a sudden emergency stop, recording the temporal signals and performing a spectral analysis of them (figures 15 and 16). As can be seen in the temporal signals, the response corresponds to that of a free vibration. damped, in which the structure has been momentarily excited, then an emergency stop is executed, so that the structure vibrates freely until it comes to a complete stop.

The spectral analysis reveals that the frequency content in both cases is practically the same, corresponding to the different natural frequencies that have been excited and that determine, together with the modal shapes, the dynamic response of the structure. It is also observed that the amplitudes of the FFT frequencies in signal 1 and signal 2 in the first two modes differ. This may be due to the fact that the acceleration in signal 1 is 33% percent greater than in signal 2, increasing the torque of the motor and causing greater torque forces on flange 2B.

Taking into account that the accelerometers are measuring in the Z direction, the comparison made in table 5 between the frequencies identified experimentally and those obtained numerically through the FEA analysis shows how the stiffness value of the 2B flange corresponding to a material with an elastic modulus equivalent to steel is the one with the best fit. Thus, by using such stiffness value, the adjustment presents the smallest difference for the 2nd frequency mode, which is the one that mobilizes the most mass in the measurement direction (Z axis), showing -0.66 % error. In addition, the average error for the rest of the modes, ignoring 6th mode, which practically does not mobilize mass in the Z direction, is also the lowest, showing differences that vary between 11.6% for 1st mode and 1.7% for 5th mode, which is the second mode that mobilizes more mass in the Z axis.

The order of magnitude of the differences in the values of the frequencies obtained between the FEA and the spectral analysis in our study are consistent with the results obtained by Worthington et al. [7]. In their work, they made a simplified FEM model of the tracker bridge for the Hobby-Eberly Telescope, obtaining the modes and natural frequencies using FEA. Subsequently, they experimentally determined the natural frequencies and modes by exciting the structure with an impact hammer and measuring the response with accelerometers. The differences obtained between the experimental measurements and the numerical model were 6.16% in the 1st mode, 0.55% in the 2nd mode and 12.43% in the 3rd mode.

In [11], the displacement of the CCD in the JAST80 telescope in the Z direction was studied, as in the experiments carried out in this work. The conclusions determined that the maximum displacements of the CCD occurred for frequencies around 7 Hz, coinciding with the first natural frequency of the structure.

The Hobby-Eberly Telescope Wide-Field [7], the New Robotic Telescope (NRT) [8] and the JST/T250 telescope pier adjacent to the JAST80 [3] share an altazimuth mount having (by design) an imposed resonance frequency as the 1st mode of 10 Hz. In the JAST80 telescope it is observed that the elasticity of the mount is more flexible than in the previous cases, this may be due to the geometry of the mount and the positioning of the telescope, since it is suspended. On the contrary, the altazimuth mounts have two supports that support it on a rotating base. This geometry without counterweights gives the mount-telescope assembly greater rigidity.

E. Analysis of movements in normal operation

The results of the frequency analysis of the AR movement signal in slewing mode are shown in figure 17 (STFT is depicted) and in figure 18 (FFT is depicted). In both signals, the frequency component of 50 Hz is observed, corresponding to the electric current component, while the amplitudes for the natural frequencies are low with respect to the amplitudes obtained in free vibration due to a sudden emergency stop.

In the spectral analysis using STFT, the natural frequencies associated with the first modes obtained through the FEA analysis are the ones that predominate compared to the frequencies of the 5th and 6th modes, concentrating on the beginning and end of the displacement, which coincide with the acceleration periods of the actuator to reach the constant

speed of the movement and the deceleration period until it stops.

The conditions for the mount to vibrate in resonance due to the vibrations produced by the actuator depend on whether their frequencies coincide with the natural frequencies of the mount and, furthermore, their amplitude is sufficient to significantly excite them.

We conclude that the natural frequencies calculated by FEA are present in the vibrational response of the mount, but their amplitude is not decisive in the vibrations that reach the instrumentation because they are not sufficiently excited by the nature of the movement. This can be corroborated if we compare the amplitude of the frequency lobes belonging to a movement with a sudden emergency stop (figure 15), with the amplitude of the FFT lobes of the movement in normal operation (figure 18).

V. Conclusion

In this work we have validated a simplified FEM model of the JAST80 telescope mount by means of the natural frequencies calculated by FEA and the spectral analysis of the vibrations in the instrumentation by excitation of a free movement after an unexpected emergency stop of the telescope. As far as the AR movement in normal operation is concerned, the frequency amplitudes obtained by spectral analysis are not relevant with respect to the validated simplified FEM natural frequencies.

The obtained results open the door to interesting applications. The first one is based on a predictive maintenance of the structure. This idea has been recently implemented by Guo et al. [29] aimed at predicting the remaining useful life (RUL) of rolling bearings. Meng et al. [30] also proposed two novel health monitoring indicators based on multifeatures of envelope spectrum for health condition monitoring of bearings, including determining the initial fault, assessing and degradation of bearing. We found other examples of potential methods for structural health monitoring in civil structures such a suspension bridge [16]. In our case, it is possible to study (by means of spectral analysis) the vibrations captured by the accelerometers in the same movement carried out over a wide time interval. The deviations of the main lobes (natural frequencies) of the spectral analysis at frequencies lower than those initially measured, could indicate the degradation of the structural integrity or an increase in the existing clearances, implying a decrease in its rigidity and therefore a decrease in the natural frequencies.

Another interesting line of work that we intend to carry out is based on the use of the developed FEM model to obtain a mathematical model. The objective would be to modify the control loop of the actuator that controls the AR movement by introducing the mathematical model. In this way, the vibrations that reach the instrumentation could be dampened, thus optimizing the speed and acceleration parameters. The same way that Reinacher et al. used the vibrational response measured by the Focal Plane Imager camera to design the control system of SOFIA telescope [31].

Acknowledgment

This work has been supported by the Observatorio Astrofísico de Javalambre (OAJ), in Teruel, a Spanish Infraestructura Cientifico-Técnica Singular (ICTS) owned, managed and operated by the Centro de Estudios de Física del Cosmos de Aragón (CEFCA).

References

[1] G. Palacios-Navarro, F. Arranz Martínez, R. Martín Ferrer, and P. Ramos Lorente, “Compensation Techniques Aimed at Mitigating Vibrations in Optical Ground-Based Telescopes: A Systematic Review,” Sensors, vol. 21, no. 11, Art. no. 11, Jan. 2021, doi: 10.3390/s21113613.

[2] P. Gatkine and B. Kumar, “Dynamical modeling and resonance frequency analysis of 3.6 m optical telescope pier,” Int. J. Struct. & Civil Engg. Res., vol. 3, no. 1, pp. 1–10, Apr. 2014.

[3] S. François, P. Galvín, P. Museros, G. Lombaert, and G. Degrande, “Dynamic soil–structure interaction analysis of a telescope at the Javalambre Astrophysical Observatory,” Soil Dynamics and Earthquake Engineering, vol. 65, pp. 165–180, Oct. 2014, doi: 10.1016/j.soildyn.2014.06.014.

[4] D. G. MacMynowski, G. Z. Angeli, K. Vogiatzis, J. Fitzsimmons, and S. Padin, “Parametric modeling and control of telescope wind-induced vibration,” USA, Sep. 2004, p. 266. doi: 10.1117/12.552282.

[5] F. Zhao, P. Wang, Y. Gong, L. Zhang, C. Meng, and J. Lin, “Numerical simulation of airflow in a 2m telescope,” Chengdu, China, May 2009, p. 72810K. doi: 10.1117/12.831445.

[6] Y. Lammen, A. Reinacher, B. Greiner, J. Wagner, and A. Krabbe, “Increasing the SOFIA Secondary Mirror Mechanism’s Fast Steering Capability by Identification of a Structural Resonance and Its Subsequent Elimination Through Mass Re-Distribution,” J. Astron. Instrum., vol. 07, no. 04, p. 1840001, Dec. 2018, doi: 10.1142/S2251171718400019.

[7] M. S. Worthington, N. T. Mollison, I. M. Soukup, J. J. Zierer, J. M. Good, and S. P. Nichols, “Design and analysis of the tracker bridge for the Hobby-Eberly Telescope wide-field upgrade,” in SPIE Astronomical Telescopes + Instrumentation, San Diego, California, USA, Jul. 2010, p. 773341. doi: 10.1117/12.857090.

[8] A. Ranjbar et al., “Conceptual design of a fast-slewing mount for the New Robotic Telescope,” in Ground-based and Airborne Telescopes VIII, Yokohama, Japan, Dec. 2020, vol. 11445, pp. 975–985. doi: 10.1117/12.2561320.

[9] X. Qiao, G. Ding, X. Chen, P. Cai, and L. Shao, “Comparison of 3-D Self-Calibration Methods for High-Precision Measurement Instruments,” IEEE Trans. Instrum. Meas., vol. 71, pp. 1–9, 2022, doi: 10.1109/TIM.2022.3149090.

[10] X. Li et al., “A New Mechanical Resonance Suppression Method for Large Optical Telescope by Using Nonlinear Active Disturbance Rejection Control,” IEEE Access, vol. 7, pp. 94400–94414, 2019, doi: 10.1109/ACCESS.2019.2928050.

[11] A. J. Cenarro et al., “J-PLUS: The Javalambre Photometric Local Universe Survey,” A&A, vol. 622, p. A176, Feb. 2019, doi: 10.1051/0004-6361/201833036.

[12] C. Mendes de Oliveira et al., “The Southern Photometric Local Universe Survey (S-PLUS): improved SEDs, morphologies, and redshifts with 12 optical filters,” Monthly Notices of the Royal Astronomical Society, vol. 489, no. 1, pp. 241–267, Oct. 2019, doi: 10.1093/mnras/stz1985.

[13] F. Arranz Martínez, R. Martín Ferrer, G. Palacios-Navarro, and P. Ramos Lorente, “Study on the Vibration Characteristics of the Telescope T80 in the Javalambre Astrophysical Observatory (JAO) Aimed at Detecting Invalid Images,” Sensors, vol. 20, no. 22, p. 6523, Nov. 2020, doi: 10.3390/s20226523.

[14] V. P. Smekalin, V. N. Fedoseyev, Yu. I. Shanin, and D. A. Yagnyatinskiy, “Finite Element Analysis of the Structural Mechanics of the Telescope Objective for the Lira-B Space Experiment,” Optoelectron.Instrument.Proc., vol. 55, no. 5, pp. 525–534, Sep. 2019, doi: 10.3103/S8756699019050170.

[15] J. Sebag et al., “LSST telescope modeling overview,” in SPIE Astronomical Telescopes + Instrumentation, Edinburgh, United Kingdom, Aug. 2016, p. 99112E. doi: 10.1117/12.2233178.

[16] K.-S. Lim, M. K. A. Zaini, Z.-C. Ong, F. Z. M. Abas, M. A. B. M. Salim, and H. Ahmad, “Vibration Mode Analysis for a Suspension Bridge by Using Low-Frequency Cantilever-Based FBG Accelerometer Array,”

IEEE Trans. Instrum. Meas., vol. 70, pp. 1–8, 2021, doi: 10.1109/TIM.2020.3018578.
[17] J. Wu, X. Zhang, and B. Li, “A study on vibration component separation of a rotor system during startup and its application in fault diagnosis,” Meas. Sci. Technol., vol. 30, no. 9, p. 095104, Sep. 2019, doi: 10.1088/1361-6501/ab199c.
[18] P. Romano and M. Paolone, “Enhanced Interpolated-DFT for Synchrophasor Estimation in FPGAs: Theory, Implementation, and Validation of a PMU Prototype,” IEEE Trans. Instrum. Meas., vol. 63, no. 12, pp. 2824–2836, Dec. 2014, doi: 10.1109/TIM.2014.2321463.
[19] D. Belega and D. Petri, “Accuracy Analysis of the Multicycle Synchrophasor Estimator Provided by the Interpolated DFT Algorithm,” IEEE Trans. Instrum. Meas., vol. 62, no. 5, pp. 942–953, May 2013, doi: 10.1109/TIM.2012.2236777.
[20] M. Caza-Szoka and D. Massicotte, “Windowing Compensation in Fourier Based Surrogate Analysis and Application to EEG Signal Classification,” IEEE Trans. Instrum. Meas., vol. 71, pp. 1–11, 2022, doi: 10.1109/TIM.2022.3149325.
[21] A. Elsonbaty, A. Allagui, and A. S. Elwakil, “Extended Instantaneous Spectral Analysis (E-ISA) for Advanced Signal Processing,” IEEE Trans. Instrum. Meas., vol. 71, pp. 1–10, 2022, doi: 10.1109/TIM.2022.3165267.
[22] D. Gabor, “Theory of communication. Part 1: The analysis of information,” Journal of the Institution of Electrical Engineers - Part III: Radio and Communication Engineering, vol. 93, no. 26, pp. 429–441, Nov. 1946, doi: 10.1049/ji-3-2.1946.0074.
[23] D. Giagopoulos, A. Arailopoulos, V. Dertimanis, C. Papadimitriou, E. Chatzi, and K. Grompanopoulos, “Structural health monitoring and fatigue damage estimation using vibration measurements and finite element model updating,” Structural Health Monitoring, vol. 18, no. 4, pp. 1189–1206, Jul. 2019, doi: 10.1177/1475921718790188.
[24] P. Langer, C. Jelich, C. Guist, A. Peplow, and S. Marburg, “Simplification of Complex Structural Dynamic Models: A Case Study Related to a Cantilever Beam and a Large Mass Attachment,” Applied Sciences, vol. 11, no. 12, p. 5428, Jun. 2021, doi: 10.3390/app11125428.
[25] A. Thakur, A. G. Banerjee, and S. K. Gupta, “A survey of CAD model simplification techniques for physics-based simulation applications,” Computer-Aided Design, vol. 41, no. 2, pp. 65–80, Feb. 2009, doi: 10.1016/j.cad.2008.11.009.
[26] Y. Zhu, Y. Huang, Y. Li, Z. Qiu, and Z. Zhao, “A Smartphone-Based Six-DOF Measurement Method With Marker Detector,” IEEE Trans. Instrum. Meas., vol. 71, pp. 1–14, 2022, doi: 10.1109/TIM.2022.3200432.
[27] K. Fujita and N. Kuramoto, “Finite-Element Simulation of Effect of Surface Roughness of Coaxial Cylindrical Electrodes on Small Mass and Force Measurements Using Voltage Balance Apparatus,” IEEE Trans. Instrum. Meas., vol. 71, pp. 1–6, 2022, doi: 10.1109/TIM.2022.3165249.
[28] B. N. Parlett and D. S. Scott, “The Lanczos algorithm with selective orthogonalization,” Math. Comp., vol. 33, no. 145, pp. 217–238, 1979, doi: 10.1090/S0025-5718-1979-0514820-3.
[29] R. Guo, Y. Wang, H. Zhang, and G. Zhanga, “Remaining Useful Life Prediction for Rolling Bearings Using EMD-RISI-LSTM,” IEEE Trans. Instrum. Meas., pp. 1–1, 2021, doi: 10.1109/TIM.2021.3051717.
[30] J. Meng, C. Yan, G. Chen, Y. Liu, and L. Wu, “Health Indicator of Bearing Constructed by rms-CUMSUM and GRRMD-CUMSUM With Multifeatures of Envelope Spectrum,” IEEE Trans. Instrum. Meas., vol. 70, pp. 1–16, 2021, doi: 10.1109/TIM.2021.3054000.
[31] A. Reinacher et al., “The SOFIA Telescope in Full Operation,” J. Astron. Instrum., vol. 07, no. 04, p. 1840007, Dec. 2018, doi: 10.1142/S225117171840007X.